

1
2
3
4
5
6
7
8
9
10
11
12
13

Observations of the Roots of Plasma Bubbles: Are They Sometimes Foamy?

Charles L. Bennett¹

¹Lawrence Livermore National Laboratory (retired).

Corresponding author: Charles Bennett (Charlie_Bennett@comcast.net)

Key Points:

- Dispersionless, highly attenuated, lightning generated electromagnetic waves are observed in the lower ionosphere
- The propagation of these electromagnetic waves has characteristics of acoustic wave propagation through two-phase foams
- Such foamy plasma bubbles may cover approximately 80% of the bottomside of the equatorial nightside ionosphere.

14 **Abstract**

15 Dramatic irregularities in the plasma density of the ionosphere, first discovered by their effects
16 on radio wave propagation in 1938, and despite decades of investigation, still remain puzzling.
17 Their deleterious effects on radio wave communication, satellite command and control, GPS
18 navigation are serious enough to strongly motivate better understanding of their nature. Many
19 aspects of such irregularities are now understood, but the mechanism(s) of their formation and
20 their detailed nature remain a topic of great interest. In this work, detailed time resolved
21 measurements of lightning generated waves show dispersionless, strongly attenuated propagation
22 with substantial propagation delays. These characteristics of the electromagnetic wave
23 propagation in the two-phase bubble/non-bubble ionosphere parallel the characteristics of
24 acoustic wave propagation through two-phase liquid/vapor foams; and this motivates the
25 suggestion that the bottomside layer of the ionosphere may sometimes be foamy.

26 **Plain Language Summary**

27 Just as ocean waves breaking at the interface between sea and land produce copious bubbles and
28 foam, recent satellite data suggests a similar phenomenon at the interface between neutral
29 atmosphere and the charged plasma of the ionosphere. Lightning generated electromagnetic
30 waves passing through the lower ionosphere observed by low altitude satellites are found to have
31 the same characteristics as acoustic waves passing through foamy water. This hypothetical foam
32 in the lower ionosphere apparently strongly absorbs radio waves and seems to prevent most such
33 waves from escaping the foam to pass through to the upper ionosphere.

34 **1 Introduction**

35 This article is a sequel to (Bennett, 2023), that describes a novel method for the
36 observation and analysis of the *roots* of equatorial plasma bubbles (EPBs). Most of the details in
37 (Bennett, 2023) will not be repeated here, but a brief summary is presented in the following
38 section 2.

39 EPBs are localized density depletions (sometimes by over four orders of magnitude
40 relative to the surrounding plasma) in the nighttime equatorial ionosphere (Heelis, 2004; Kil &
41 Heelis, 1998; Woodman & Hoz, 1976). The literature on EPBs is vast and spans nearly a
42 century. Nowadays there is increasing motivation to understand such bubbles and their
43 detrimental affects on radio communications, especially satellite communications, for which
44 “loss of lock” events can be precipitated by their presence. Another detrimental effect is the
45 disruption of signals from the Global Navigation Satellite System so important to modern
46 society. Numerous reviews of the development of the experimental and theoretical understanding
47 of plasma bubbles are available (e.g. Balan et al., 2018; De Michelis et al., 2021; Huba, 2023;
48 Kelley et al., 2011; Makela & Otsuka, 2012; Woodman, 2009).

49 It is generally accepted that the lower density of plasma bubbles relative to their
50 surroundings causes them to rise in a turbulent process giving rise to plumelike features in radar
51 observations (e.g. Abdu et al., 2012; Hysell et al., 2005; Kelley et al., 2011; Kudeki &
52 Bhattacharyya, 1999; Narayanan et al., 2014; Patra et al., 2005; Tsunoda, 1983; Yokoyama et al.,
53 2011). Plasma bubbles may also be detected as emission depletion bands in optical observations,
54 (e.g., Immel et al., 2003; Kil et al., 2004; Makela & Kelley, 2003; Makela et al., 2006; Makela &
55 Miller, 2008; Martinis et al., 2003; Mendillo & Baumgardner, 1982; Pimenta et al., 2003;
56 Shiokawa et al., 2004). Animations of sequences of optical images, such as those in Makela and

57 Miller (2008) most clearly and dramatically show plasma bubbles emerging from low altitudes
58 with subsequent rising and Eastward drifting. Such animations not only show apparent turbulent
59 structures emerging from regions of depleted emission, but also show apparently non-turbulent
60 depleted emission regions extending continuously below the turbulent regions towards the base
61 of the ionosphere. In the present article the term *roots* of plasma bubbles refers to density
62 depletions that extend *contiguously* to the base of the ionosphere that aren't necessarily turbulent.
63 It is beyond the scope of this article to explain exactly how these density depletions are formed.

64 Initial observations and most early investigations of plasma bubbles involved so-called
65 “spread F” phenomena, in which radar pulses of a given frequency, rather than reflecting from
66 distinct ionospheric layers corresponding to distinct altitudes of reflection were observed to
67 return from a spread out region of altitudes (Woodman, 2009). As such radar reflections require
68 the presence of ionospheric density irregularities at the scale of the radar wavelength,
69 conventional spread F phenomena would not be seen for non turbulent roots of plasma bubbles.

70 Woodman (2009) states “We implicitly assume that there is a cascade mechanism as
71 proposed by Haerendel (1973) from the larger to the smaller scale, but we do not know exactly
72 how this takes place.” Woodman (2009) further states “The current state of the theory is that
73 high frequency drift instabilities can explain the shortest wavelengths, up to ~1 m and the low
74 frequency waves longer than 10 m, but no existing theory can explain the waves around 3 m, i.e.,
75 the strong echoes that Jicamarca sees!”

76 Kelley (2011) states “How structure can be transferred from 1000 km to 1 m is still a bit
77 of a mystery. Since there is linear growth in the power law regime, it is not because of an inertial
78 cascade” and “Much remains to be done before the electrodynamic and coupling processes in
79 this region during solar minimum conditions are fully understood.”

80 To this day, the formation of the initial density depletions evidently required to “seed”
81 larger scale turbulent fluctuations responsible for the greatest degradations of radio
82 communications are not fully understood (Chou et al., 2022; De Michelis et al., 2022; Huba,
83 2023; Kil et al., 2022).

84 The remainder of this paper is organized as follows: Section 2 provides a summary of the
85 earlier (Bennett, 2023) paper involving the detailed description of the data sources and analysis
86 methods relevant to the current work. The main new results in the current work involve the
87 detailed wavevector analysis of both dispersed (i.e. whistlers) and unusually low dispersion
88 waves. In addition, previously unnoticed “precursors” to the unusually low dispersion waves are
89 identified and described. Normally dispersed waves are discussed in section 3. In section 4
90 unusually low dispersion waves are discussed. Section 5 presents a physical model for “foamy”
91 plasma. The various observations in (Bennett, 2023) and the new observations in the present
92 paper are interpreted in terms of this model. Section 6 provides further discussion and
93 conclusions.

94

95 **2 Highlights of Earlier Work and New Observations**

96 In (Bennett, 2023) I suggested that the roots of plasma bubbles might sometimes be
97 foamy. This suggestion was made based on the propagation characteristics of lightning generated
98 (LG) waves passing through such roots and in analogy to the propagation of acoustic waves
99 through mixed liquid/gas phase foamy media. A specific model of the propagation of

100 electromagnetic waves through such “plasma foam” at the bottom of the ionosphere will be
101 discussed in Section 5.

102 In Figure 1, a slightly expanded region of that shown in Figure 11 of (Bennett, 2023), the
103 electric field signals observed by the EMFISIS instruments on the Van Allen Probe (VAP)
104 satellite at 2.5°S 154.6°W altitude 239 km from a single lightning flash located at 9.2°N 84.8°W,
105 comprising four strokes, are shown. In Figures 1b, 1d and 1f, the temporal variations of the
106 electric field components E_u , E_v and E_w along the three axes, U, V and W of the spinning VAP
107 satellite are shown. The W axis is spin aligned and approximately vertical here. Figures 1a, 1c
108 and 1e display scalograms for the three electric field components computed using a continuous
109 wavelet transform (CWT) as described in (Bennett, 2023). Scalograms display the time
110 dependence of the frequency components of a waveform and feature higher temporal resolution
111 at higher frequencies following the cone of influence (COI) function. An example of the COI
112 function centered at the time of the second pulse is shown in Figure 1e by the white curved
113 dashed line. An impulsive disturbance at a single time sample in the electric field would produce
114 a scalogram peak with the shape of the COI. The COI also indicates how data outside the time
115 period used in the CWT may affect the scalograms. The COI of the boundary effects is shown as
116 a curved black dashed line in 1a, 1c and 1d. Scalogram values at frequencies below the boundary
117 COI are unreliable. For example, in 1a and 1c, at the start of the time period, the greenish region
118 below the COI is a boundary artifact.

119 The appearance times of the four peaks seen in Figure 1f, are delayed by 20, 31, 30 and 7
120 ms as indicated above Figure 1e relative to the arrival times of LG pulses at the subsatellite
121 location. The curve shown in Figure 1g is the sum of the waveforms from the Nickolaenko et al.
122 (2004) model using parameters for the stroke intensities and arc distances from the subsatellite
123 position to the stroke location detected by the World Wide Lightning Locator Network
124 (WWLLN) over the time period shown. WWLLN is a global Very Low Frequency (VLF; 3-
125 30kHz) lightning location system capable of finding the radiated energy, time and location of
126 individual lightning strokes with ~ 10 km spatial accuracy, ~ 10 μ s temporal accuracy and $\sim 90\%$
127 efficiency for high peak current strokes (Abarca et al., 2010; Holzworth et al., 2019; Hutchins et
128 al., 2012; Jacobson et al., 2006; Rodger et al., 2006). Red vertical lines in Figures 1b, 1d and 1f
129 mark the three peaks in the composite model electric field function shown in Figure 1g. The
130 (Nickolaenko et al., 2004) model propagation speed of 245 km/s accurately matches the
131 observed travel speed 245 ± 5 km/s for ELF pulses observed at ground level by the World ELF
132 Radiolocation Array (WERA), as discussed by (Bennett, 2023) and shown in Figure 10 of that
133 article. The propagation speed of LG pulses through the Earth Ionosphere waveguide (EIWG) is
134 primarily a function of the altitude of the EIWG upper boundary (EIWGUB) as discussed in
135 (Golkowski et al., 2018). All of the VAP data in this article were acquired near local midnight,
136 so that most of the stronger LG pulses travelled entirely through regions with higher EIWGUB
137 altitudes. The second of the four pulses seen in Figure 1f was detected in the Geostationary
138 Lightning Mapper (GLM) (Bateman et al., 2020; Goodman et al., 2013; Rudlosky et al., 2019)
139 data, but not in the WWLLN data.

140 A feature of the data shown in Figure 1c that was not noticed by (Bennett, 2023) is the
141 presence of two “Precursor” streaks most clearly seen in the E_v scalograms near 10 kHz. These
142 precursors first appear approximately 4 ms after the red vertical lines in Figure 1a-1f. A similar
143 precursor is only marginally apparent preceding the fourth peak and no significant precursor
144 appears before the second pulse in Figure 1f. Examination of other VAP data bursts reveals that

145 such precursors often do appear, albeit only in a minority of the cases for which clear, well
 146 identified LG peaks are seen in the scalograms. In numerous other cases, such precursors are
 147 found very well correlated with the subsatellite arrival time of EMPs predicted using the
 148 Nickolaenko et al. (2004) model and WWLLN measured times and locations. In the first nine
 149 figures in the Supplemental materials **S1**, 22 distinct examples of precursors may be seen.

150 Another significant example involving multiple strokes from a single lightning flash is
 151 shown in Figure 2. In this case, a single flash at 12.7°N 152.8°E comprising three WWLLN
 152 strokes occurring in rapid succession produces three precursors and three bipolar pulses in the
 153 electric field components. The bipolar pulses are narrowest in the E_v component and broadest in
 154 the E_u component. The precursors in this case appear strongest in the E_u component, are
 155 significant in the E_v component but lost in the noise in the E_w component. The relatively broad
 156 temporal extent of the precursors suggests that they may be a novel form of spread F, but seen at
 157 frequencies far below radar frequency and in terms of direct propagation delay rather than as
 158 reflected pulses. Validation of the assumed 245 km/s group velocity for propagation through the
 159 EIWG in this case is validated by the WERA data for these LG pulses shown in the last three
 160 figures in the Supplemental materials.

161 Despite the substantial propagation delays for the LG events seen in Figures 1f and 2d,
 162 no significant increase in the widths of the pulses (relative to the model pulses in Figures 1g and
 163 2g) from the propagation through the EIWG from the location of the lightning flash to the
 164 subsatellite point was seen. This dispersionless propagation of LG EMPs through the lower
 165 ionosphere exemplified by Figures 1 & 2 is in stark contrast to the characteristics of normal
 166 whistlers. In the following section 3, the detailed behavior of normal whistlers is quantitatively
 167 described. In section 4, unusual dispersion events are discussed. A possible physical explanation
 168 of both the “spread F like” precursors and the delayed bipolar dispersionless pulses will be
 169 discussed in Section 5.

170

171 **3 Wave Vector Analysis for Normal Whistler Events**

172 **3.1 Normal Two Fluid Plasma Dispersion Relations**

173 In (Bennett, 2023) it was empirically found, for propagation angles θ relative to the local
 174 magnetic field not close to $\pm 90^\circ$, that both the phase and group velocities versus frequency of
 175 fast magnetosonic “whistler” waves for frequencies above the relevant ion cyclotron frequency
 176 and below the electron cyclotron frequency have a square root dependence on frequency
 177 insensitive to ion mass. Numerically the group velocity vs. frequency is approximately

178

$$179 \quad V_{group} = 189 \frac{km}{s\sqrt{Hz}} \sqrt{\frac{75 \text{ mm}^{-3}}{N_e} \frac{B}{31 \mu T}} \sqrt{f} , \quad (1)$$

180

181 while the phase velocity is approximately

182

$$V_{phase} = 112 \frac{km}{s\sqrt{Hz}} \sqrt{\frac{75 mm^{-3}}{N_e} \frac{B}{31 \mu T}} \sqrt{f \cos(\theta)} . \quad (2)$$

184
185 These general and characteristic features of the classical whistler portion of the dispersion
186 relations (De Jonghe & Keppens, 2021b) are seen in observational data for whistlers in “normal”
187 plasma regions, but are *violated* in regions of unusual dispersion.
188

189 3.2 Normal Dispersion Relation Observations

190 Figure 3 of the present work shows the scalograms from a 1.6 second portion of the
191 scalograms shown in Figure 5 of (Bennett, 2023). The overall travel time, including the
192 propagation time through the EIWG to the subsatellite location, ΔT_0 , followed by the passage
193 upwards through the ionosphere to the satellite detectors is given by the integral of the inverse
194 group velocity over the path length as

$$195 \Delta T = \int \frac{ds}{v_{group}(s)} = \Delta T_0 + DC / \sqrt{f} . \quad (3)$$

197
198 In the equality on the right hand side of expression (3), the dispersion constant (DC)
199 value implicitly represents the integral over all variations along the path *through the ionosphere*
200 of the factors in expression (1). Superimposed over the scalograms in Figure 3, the white vertical
201 dashed line shows the arrival time of an LG pulse at a time ΔT_0 after the WWLLN observed
202 stroke time. The three curved red dashed lines show three dispersion curves having DC values of
203 0.1, 12 and 24 $s\sqrt{Hz}$, and having the same arrival time at the subsatellite location as the white
204 dispersionless case. For DC values much less than 0.1 $s\sqrt{Hz}$, *normal* whistlers appear effectively
205 dispersionless, arriving at a time ΔT_0 after the associated lightning stroke.

206 3.3 Wavevector Analysis of Normal Dispersion Observations

207 Figure 4 of the present work shows a wave vector analysis using the amplitudes along the
208 four superimposed dispersion curves indicated by dashed lines in Figure 3. At each frequency
209 and time along the dispersion curves having DC values indicated in the column titles for Figures
210 4a, 4f, 4k and 4p, the complex amplitudes of the scalograms for the electric and magnetic fields
211 are used to compute the Poynting vector

$$212 \mathbf{S}(f) = \mathbf{E}(f) \times \mathbf{B}^*(f) , \quad (4)$$

213
214
215 and the unit Poynting vector

$$216 \hat{\mathbf{S}}(f) = \mathbf{S}(f) / |\mathbf{S}(f)| . \quad (5)$$

218

219 The absolute values of the scalar product of the unit Poynting vector with each of the unit
 220 vectors in the mean field aligned (MFA) coordinate system described in (Min et al., 2017; Ritter
 221 et al., 2013) as a function of frequency are shown in the top three rows of Figure 4. The MFA
 222 coordinate labels here (μ , ϕ , and ν) follow the notation of Min et al. (2017). The scalar products
 223 along the local magnetic field are indicated by $|\mathbf{S} \cdot \boldsymbol{\mu}|$ in the ordinate label in 4a. The scalar
 224 products along the magnetic East direction in the horizontal plane are indicated by $|\mathbf{S} \cdot \boldsymbol{\phi}|$ in the
 225 ordinate label in 4c. The scalar products along the direction orthogonal to the first two
 226 directions, approximately vertical in the equatorial region, are indicated by $|\mathbf{S} \cdot \boldsymbol{\nu}|$ in the ordinate
 227 label in 4b. In 4d, 4i, 4n and 4s, the absolute value of the electric and magnetic field scalogram
 228 components are shown as a function of frequency. The random phase approximation (RPA) for
 229 the phase velocity as a function of frequency is computed according to the method described by
 230 (Bennett, 2023) from the complex scalogram amplitudes along each of the four dispersion curves
 231 shown in Figure 3, and is plotted in Figure 4e, 4j, 4o and 4t.

232 Expression 2 is used to estimate the propagation angles θ in Figure 4e, 4j, 4o and 4t by
 233 fitting the high frequency behavior of the four cases. These estimated angles are shown in blue in
 234 the last row of Figure 4 and the phase velocity vs. frequency variation of expression 2 is shown
 235 by the green line in Figure 4e, 4j, 4o and 4t above the oxygen cyclotron frequency. Below the
 236 oxygen cyclotron frequency the phase velocity is shown by the horizontal section of the green
 237 line at its long wavelength limit assuming the plasma is predominantly O^+ ions.

238 Since the “noise” of other contributions to the scalogram amplitudes along the four
 239 dispersion curves is not negligible, significant fluctuations are seen in the estimated Poynting
 240 vector projections displayed in the top three rows of Figure 4. Even so, it seems the direction of
 241 the *energy* flow for the low dispersion whistler and its echos are traveling in approximately
 242 consistent directions, in contrast to the apparent variation in the direction of the *wavevector*
 243 suggested in the last row of Figure 4. The sign of the energy propagation direction is irrelevant in
 244 the plots of the absolute values of the energy propagation direction cosines shown in the top
 245 three rows of Figure 4. This whistler and its echos are travelling obliquely in the MFA
 246 coordinate system, with unit Poynting vector projections of approximately 0.8, 0.5 and 0.4 along
 247 the $\boldsymbol{\mu}$ (magnetic field B), $\boldsymbol{\nu}$ (\sim vertical), and $\boldsymbol{\phi}$ (magnetic East) directions.

248

249

250 Even though the dispersion constant (DC) values are dramatically different for the four
 251 cases displayed in Figure 4, the RPA estimated phase velocities for all four cases are not so
 252 different, and are consistent with slightly different $\cos(\theta)$ angular factors. The reason for the
 253 great differences between the DC values is that they represent integrated totals of the dispersion
 254 over the full distance (in the last two cases including the echoing path) from source to detector.
 255 This sensitivity of the DC values to the integrated dispersion along the full path from source to
 256 detection was extensively exploited and discussed in (Bennett, 2023). In contrast, the four
 257 dispersiveness coefficients (50, 50, 80 & 112) in the legends in 4e, 4j, 4o and 4t are local
 258 measurements, characteristic of the conditions of the ionosphere at the location of the detectors,
 259 rather than an integral measure along the full propagation path.

260 Finally, some measure of the fidelity of the RPA estimates for phase velocity can be
 261 judged by the degree to which the scalograms are found to have significant values above the

262 ambient “noise”. For example, for the Bu component displayed in **3a**, scalogram amplitudes for
 263 frequencies below 100 Hz appear to decrease to the level of the “background” amplitudes
 264 primarily associated with the population of slow magnetosonic waves discussed in (Bennett,
 265 2023). Other components are similarly “lost” in the background noise at a variety of frequency
 266 levels. As a guide for the interpretation of which frequencies have meaningful values for both the
 267 direction projections shown in the top three rows, and the phase velocities shown in the bottom
 268 row of Figure 4, the cyclotron frequencies for Oxygen and Hydrogen are shown by the white and
 269 magenta dashed lines in Figure 3 and cyan and magenta dashed lines in Figure 4 in order to more
 270 readily identify regions having significant amplitudes for all six electromagnetic components.

271 **4 Wave Vector Analysis for Unusual Dispersion Events**

272 4.1 A Region of Unusual Dispersion

273 Figure 5 of the present work shows the scalograms from a single data burst acquired
 274 shortly before the burst scalograms shown in Figure 9 of (Bennett, 2023). In this figure, the
 275 arrival times of EMPs from every lightning strike detected by the WWLLN are shown by the
 276 vertical dashed white lines. Not a single normally dispersed whistler is observed during this data
 277 burst. This data has the character described in (Bennett, 2023) for periods that the Van Allen
 278 probe is passing through the root of a plasma bubble contiguously connected to the EIWG.
 279 Specifically,

- 280 1. the dispersion constant (DC) values become anomalously small relative to the
 281 estimate from the international reference ionosphere (IRI) model for the time and
 282 location of the satellite,
- 283 2. it is observed that the “spikes” in the scalograms corresponding to anomalously small
 284 DC values do not extend much above 1 kHz, in contrast to normal, very low
 285 dispersion cases outside plasma bubble regions that extend all the way to the Nyquist
 286 frequency as seen in Figure 3,
- 287 3. the electric field fluctuations become enhanced by several orders of magnitude
 288 relative to typical values seen just before or just after entering the bubble region,
- 289 4. the magnetic field fluctuations are not especially enhanced relative to typical values
 290 outside the bubble region,
- 291 5. where both electric and magnetic field fluctuations are significant relative to their
 292 surroundings, the estimated phase velocity is orders of magnitude faster than expected
 293 relative to the IRI model estimate.

294 The last three of these points are clearly seen in the spectra, as shown by comparison of the
 295 fourth column relative to the first or third columns in Figure 7 of Bennett (2023).

296 In the first portion of the data shown in Figure 5 prior to the identified “Period of
 297 Interest”, there are a great number of dispersionless spikes seen in the electric field scalograms,
 298 most of which do not have corresponding well isolated spikes substantially above the ambient
 299 clutter noise from the ubiquitous slow magnetosonic waves (Bennett, 2023) in the magnetic field
 300 scalograms, so that a wavevector analysis of the sort described for Figure 4 is not feasible
 301 because of the high degree of “clutter noise”. The number of spikes is much greater than the
 302 number of detected WWLLN strokes during this period. Furthermore, the timing of the WWLLN

303 stroke arrivals do not line up well with the strong dispersionless spikes in the VAP data. Since
 304 the wavevector analysis shown above in Figure 4 relies on having scalogram amplitudes for all
 305 six electric and magnetic field components that are reasonably stronger than the surrounding
 306 “noise” of other waves, the region indicated by the bracket with arrows labeled “Period of
 307 Interest” has been chosen for further wavevector analysis because of the availability of
 308 significant dispersionless spikes in the magnetic field scalograms. This region is also of interest
 309 as it appears to be at the edge of a plasma bubble, since the dispersionless spikes are suddenly
 310 not seen after this period.

311

312 4.2 Scalograms from A Region of Unusual Dispersion and the Cone of Influence

313 Figure 6 shows in more detail scalograms of the three magnetic and electric field
 314 components for the bracketed region indicated in Figure 5. Superposed on the scalograms are
 315 eight white vertical dashed lines labeled #1 - #8 chosen to pass through peaks in either the
 316 magnetic or electric scalograms. The four dashed red vertical lines are drawn at the predicted
 317 arrival times of LG waves at the subsatellite location, using the WWLLN measured locations and
 318 strike times assuming a propagation speed through the EIWG of 245 km/s. For each of the four
 319 WWLLN detected waves, the angular distance from the subsatellite point to the WWLLN
 320 determined strike location is indicated in 6f by the blue text numbers.

321

322

323

324 The noisiness of the following wavevector analysis for propagation direction and phase
 325 velocity may be attributed to the variability in the contributions from the numerous other waves
 326 present at the times chosen for analysis. The cone of influence (COI) shown by the curved red
 327 dashed lines superimposed over the scalogram plots in Figure 6 shows the boundary COI, as
 328 described in section 2 above. The COI also represents the “confusion time range” over which
 329 other waves contribute to the scalogram amplitudes associated with a given peak. For example,
 330 the strongest spike in the electric field scalograms, labeled #6, spreads more broadly in time at
 331 lower frequencies just as does the COI shown by the curved white dashed line in 6d, 6e and 6f
 332 centered at peak #6.

333

334 4.8 Foamy Behavior of Unusual Dispersion Regions

335 The wavevector analysis shown in Figure 7 for cases labeled #3, #4, #5 and #8 in Figure
 336 6 displays an unusual phase velocity distribution. At frequencies below the local oxygen
 337 cyclotron frequency, the RPA estimated phase velocity is approximately 30 Mm/s for all four
 338 cases. For cases #3 and #5, above the oxygen cyclotron frequency the RPA phase velocity drops
 339 to approximately 2 Mm/s and is *approximately constant*. In contrast, cases #4 and #8 in the 2nd
 340 and 4th columns, appear to alternate between 2 Mm/s and 30 Mm/s regions.

341 The results displayed in Figures 7e and 7o are in stark contrast to the normal variation of
 342 phase velocity as a function of frequency seen in Figures 4e, 4j, 4o and 4t. In the Figure 7e and
 343 7o plots the constancy of the phase velocity above the relevant local cyclotron frequency,
 344 Oxygen in this case, cannot be explained by any normal IRI model. In general, the local plasma
 345 dispersiveness produces a phase velocity increasing as the square root of the frequency, as in

346 expression 2. Evidence that the phase velocity for these waves is not merely locally
 347 dispersionless, but also nearly dispersionless along their full path through the ionosphere to the
 348 satellite is simply that the appearance in the scalograms such as in Figures 1 or 2 is of purely
 349 vertical spikes with negligible indication of dispersion beyond the Nickolaenko et al. (2004)
 350 model, *despite substantial overall propagation delays*.

351 The ionospheric length of the propagation path followed by LG waves cannot be less than
 352 a purely vertical path of approximately 190 km from the EIWGUB to the satellite, and thus the
 353 propagation delays of 12 and 25 ms for events #1 & #2 as indicated in Figure 6a, correspond to
 354 mean speeds no less than 16 and 8 Mm/s. Although the magnetic field scalogram spikes in
 355 Figure 6a, 6b & 6c for events #1 & #2 have such high “clutter noise” that a wavevector analysis
 356 of the type shown in figure 7 is unreliable, these speeds at least do have the same order of
 357 magnitude as the RPA estimates shown in the last row of plots in Figure 7 for peaks #3, #4, #5
 358 and #8.

359

360 5 Propagation of Magnetohydrodynamic Waves Through A Model Plasma Foam

361 Even in the absence of magnetic fields or ionization, the propagation of acoustic waves
 362 through foamy mixtures of gaseous and liquid phases is complex, as discussed for example in
 363 (Benjelloun & Ghidaglia, 2021; Elias et al., 2020; Pierre et al., 2013). Remarkably, prior to
 364 experimental confirmation, in 1941 Wood, on the basis of physical arguments, argued that the
 365 speed of sound in a mixture of two fluids would be that of a single fluid having density equal to
 366 the volumetric mean density of the two fluids, and compressibility equal to the volumetric mean
 367 compressibility. In a mixture of air bubbles in water for example, the speed of sound, according
 368 to Wood’s law, may be orders of magnitude slower than the speed of sound in either water or air.
 369 This is because the mixture density is dominated by the water fraction, while the mixture
 370 compressibility is dominated by the air fraction. It has been found (Elias et al., 2020) that
 371 Wood’s law indeed reliably predicts the velocity of sound in most liquid foams *when the bubbles*
 372 *are much smaller than the acoustic wavelength*.

373 Isolated small air bubbles in water are most likely to be nearly spherical. By contrast, low
 374 density plasma bubbles embedded in higher density plasma at the bottom of the ionosphere are
 375 expected to extend along local magnetic field lines. In the model of a small region of the lower
 376 ionosphere illustrated in Figure 8, “normal” plasma is represented by the gold colored material
 377 while very low plasma density depletion bubbles are represented by voids. In this model, the
 378 bubbles are drawn with circular shapes in the plane perpendicular to \mathbf{B} , and with a random
 379 assortment of positions and diameters. The presence of the magnetic field produces a sensitive
 380 dependence on the direction of propagation of magnetohydrodynamic (MHD) waves relative to
 381 \mathbf{B} . With the local speed of sound much less than the Alfvén speed, magnetosonic waves tend to
 382 separate into fast waves moving nearly perpendicular to \mathbf{B} and slow waves moving nearly
 383 parallel to \mathbf{B} (Jackson, 1975). As the waves discussed here are fast, I consider waves moving
 384 exactly perpendicular to \mathbf{B} . Such waves propagate with a speed dependant on the sum of
 385 hydrostatic and magnetic pressures.

386 In the plane perpendicular to \mathbf{B} , the section of “foamy” plasma shown has dimensions of
 387 a single wavelength in both the East/West and Up/Down directions. With the approximation that
 388 the compressibility of normal density plasma is much less than the compressibility of low density
 389 bubbles, the speed of fast magnetosonic waves in the mixture becomes much less than the speed

390 in either normal density plasma or low density bubbles. This speed is also a sensitive function of
391 the bubble volumetric fraction, and may vary erratically from one sample to the next. The wide
392 variety of propagation delays seen in Figures 1 and 2 can be explained by this erratic variation.

393 For wavelengths shorter than the smallest of the plasma bubble radii in this model, MHD
394 waves would tend to propagate only within the circular cross section “waveguides” bounded by
395 the high conductivity plasma “walls”, as either (Jackson, 1975) transverse electric or transverse
396 magnetic modes. With a variety of bubble diameters and plasma densities within the bubbles, the
397 group velocities of short wavelength modes passing through these waveguides would also be
398 variable. The spread in the arrival times of high frequency, short wavelength waves seen in the
399 form of “precursors” in Figures 1 and 2 can be explained by this process. Because of the low
400 plasma density within these effective waveguides, the highest propagation speed may be quite
401 high, and the earliest precursor signals may appear immediately after the arrival of LG pulses at
402 the subsatellite location, as seen in the numerous examples in Figures 1 and 2 and the
403 supplemental figures.

404 Finally, the frequency spread of the “precursors” is sometimes limited to a narrow range
405 (e.g. from just below to just above 10 kHz in the Figure 1c case), but more often extends over a
406 wider frequency range (e.g. from about 1 kHz to 20 kHz in the Figure 2a case). Examination of
407 the various examples of “precursors” in the first nine supplemental figures reveals that the
408 frequency spread of the “precursors” is relatively consistent over the brief periods shown in these
409 figures. Examination of the numerous examples shown in Figures 1 and 2 and the supplemental
410 figures further reveals that the unusual, nearly dispersionless spikes in the scalograms do not
411 usually extend much above a few kHz. From the dispersion relations for fast magnetosonic waves
412 travelling in a primarily O^+ plasma, as shown in Figure 1d of Bennett (2023), this frequency
413 corresponds to wavelengths of a few km. Both the lower frequency limit of the extent of the
414 “precursors” and the upper frequency limit of the scalogram spikes suggest that the mean spacing
415 of the bubbles in Figure 8 is typically on the order of magnitude of 1 km. This model then
416 naturally explains the lower frequency bound of the “precursors” and the upper frequency bound
417 on the dispersionless scalogram spikes.

418 6 Discussion and Conclusions

419 Another characteristic of “foamy” behavior is strong attenuation. This effect is more
420 difficult to prove directly with the Van Allen probe observations. In some rare cases, such as
421 those displayed in Figures 1 and 2, multiple intense strokes of lightning are seen emerging from
422 a single location that may be identified with individual LG pulses measured by the Van Allen
423 probe detectors. With nearly identical paths traversed from source to detector, the correlation
424 between propagation delay and attenuation may be made. However, because of the inherent
425 variability in foamy plasma model illustrated in Figure 8, the uncertainties in these
426 measurements within a single burst of data are quite large. For the data shown in Figure 1, it is
427 found that an attenuation of $49\pm 22\%$ corresponds to a propagation delay of 19 ± 12 ms, while for
428 the data shown in Figure 2, an attenuation of $1\pm 0.7\%$ corresponds to a propagation delay of
429 131 ± 5 ms. These values plotted in Figure 9 provide suggestive evidence for strong attenuation of
430 fast magnetosonic waves with propagation distance through foamy plasma. A more indirect
431 manifestation of the strong attenuation of LG waves passing through such hypothetical foamy
432 plasma is the fact that most lightning strokes do not produce detectable whistler events in the
433 Van Allen probe data.

434 In (Zheng et al., 2015) a search for coincident detections of LG events by the Van Allen
435 probe satellites and the WWLLN was made. For the subset of lightning strikes within 18° of the
436 subsatellite location, only 15.3% of the strikes were detected by the Van Allen probe
437 instruments. The relatively low 15% coincidence rate found in this study could be explained by
438 the presence of underlying plasma bubble foam covering approximately 85% of the bottom of
439 the ionosphere. In (Jacobson et al., 2018) it was found that most lightning strokes were not
440 detected by the C/NOFS instruments, while occasionally there was greatly enhanced
441 transmission of LG waves to the satellite. Quantitatively, from line 6 of table 1 of (Jacobson et
442 al., 2018) listing a population of 136-thousand WWLLN strokes having predicted strong
443 Poynting vector fluence at the subsatellite point, the estimated number of coincident Vector
444 Electric Field Investigation (VEFI) whistlers, from line 13 of table 1 was only 19-thousand
445 (14%). These authors suggested that km-scale D-layer irregularities might be responsible for
446 these effects. Frequently appearing foamy plasma bubble roots of the sort discussed here in
447 connection with Figure 8 could explain both the lack of detection for most lightning strokes
448 noted by (Jacobson et al., 2018) and the occasional greatly enhanced transmission. The rare
449 enhanced transmission observations would correspond to cases for which the C/NOFS satellite
450 was either immersed in, or just above, a plasma bubble root, while the more common lack of
451 detection would correspond to foamy, strongly attenuating bubbles not extending up to the
452 C/NOFS satellite that effectively absorbed most of the LG energy. Despite the quite different
453 analysis approaches of (Zheng et al., 2015) and (Jacobson et al., 2018), their coincident rates
454 between satellite observations of whistlers and WWLLN detected lightning strokes are in
455 reasonable agreement.

456 In conclusion, it is suggested that most ($\sim 80\%$) of the bottom of the nocturnal equatorial
457 ionosphere is covered with a “foamy” layer of plasma bubbles that extend contiguously down to
458 neutral atmosphere. Whether this foam is turbulent is an open question. The detailed spatial
459 structure of this foam is an open question. The possibility of two-phase foamy structure at the
460 base of the ionosphere may complicate theoretical analyses that implicitly assume a single-phase
461 medium. Many other such questions remain open, but it is hoped that follow up observations and
462 theoretical analysis might be stimulated by the present suggestions.

463 Acknowledgments

464 This work is entirely self funded by the author. WWLLN data was purchased from the
465 University of Washington (<https://wwlln.net>). Van Allen Probe wave data used in this paper may
466 be downloaded at no cost as described in the following paragraph, and the work of the EMFISIS
467 team in its production is gratefully acknowledged. WERA data used in the preparation of this
468 paper was provided by Jerzy Kubisz of the Astronomical Observatory of the Jagiellonian
469 University, and the author thanks him and the WERA project personnel for their help in
470 understanding this data.

471

472 Open Research

473 Van Allen Probe data used in this paper can be found in the EMFISIS archive
474 (<http://emfisis.physics.uiowa.edu/data/index>). In this index file, descriptions of each of the
475 relevant data sets, including the file naming format, are provided. The specific level 2 data
476 products involved in the present work include the “WFR-waveform-continuous-burst_emfisis-

477 L2”, “WFR-spectral-matrix-diagonal_emfisis-L2”, “magnetometer_uvw_emfisis-L2”. The
 478 specific level 3 data products are “magnetometer_hires-geo_emfisis-L3”. Swarm data used in
 479 this paper is provided by the European Space Agency and can be accessed online at
 480 <https://swarm-diss.eo.esa.int>. The high rate VFM data was taken from the level 1b
 481 “latest_baselines” folder containing “MACx_HR” files for each of the three Swarm satellites.
 482 WERA data used in this paper is described in detail on the WERA project website:
 483 <http://www.oa.uj.edu.pl/elf/index/projects3.htm> and may be freely available for scientific
 484 analysis by contacting the WERA personnel. WWLLN data was purchased from the University
 485 of Washington (<https://wwlln.net>). GLM data is available at no cost from the Geostationary
 486 Operational Environmental Satellites-R Series web site (<https://www.goes-r.gov>), but the user
 487 must register to obtain the GOES-R Series GLM L2+ Data Product “GRGLMPROD” and must
 488 select an appropriate time range for data access on the web-page:
 489 https://www.avl.class.noaa.gov/saa/products/search?datatype_family=GRGLMPROD.

490

491 References

- 492 Abarca, S.F., Corbosiero, K.L., & Galarneau, T.J. Jr. (2010). An evaluation of the Worldwide
 493 Lightning Location Network (WWLLN) using the National Lightning Detection Network
 494 (NLDN) as ground truth. *Journal of Geophysical Research*, 15, D18206,
 495 doi:10.1029/2009JD013411
- 496 Abdu, M.A., Batista, I.S., Reinisch, B.W., MacDougall, J.W., Kherani, E.A., & Sobral, H.H.A
 497 (2012). Equatorial range spread F echoes from coherent backscatter, and irregularity
 498 growth processes, from conjugate point digital ionograms., *Radio Science*, 47, RS6003,
 499 doi:10.1029/2012RS005002
- 500 Akhtar, N, Hussain, S., & Mahmood, S. (2021). Nonlinear propagation of fast and slow
 501 magnetosonic waves in collisional plasmas. *Contributions to Plasma Physics*.
 502 <https://doi.org/10.1002/ctpp.202000210>
- 503 Balan, N., Liu, LiBo & Le, H. (2018). A brief review of equatorial ionization anomaly and
 504 ionospheric irregularities. *Earth and Planetary Physics*, 2, 257-275,
 505 <https://doi.org/10.26464/epp2018025>
- 506 Bateman, M., Mach, D., & Stock, M. (2020). Further investigation into detection efficiency and
 507 false alarm rate for the geostationary lightning mappers aboard GOES-16 and GOES-17.
 508 *Earth and Space Science*, 8, 2020EA001237. <https://doi.org/2020EA001237>
- 509 Benjelloun, S. & Ghidaglia, J.-M. (2021). On the sound speed in two-fluid mixtures and the
 510 implications for CFD model validation. *European Journal of Mechanics / B Fluids*, 90,
 511 152-168. <https://doi.org/10.1016/j.euromechflu.2021.09.002>
- 512 Bennett, C.L. (2023). A Novel Population of Slow Magnetosonic Waves and a Method for the
 513 Observation of the Roots of Plasma Bubbles in the Lower Ionosphere. *ESS Open Archive*.
 514 January 17, 2023, doi:10.1002/essoar.10511954.3
- 515 Chou, M.Y., Yue, J., Sassi, F., Huba, J., McDonald, S.E., Tate, J.L., et al, (2022). Modeling the
 516 Day-to-Day Variability of Midnight Equatorial Plasma Bubbles with SAMI3/WACCM-
 517 X. Authorea. December 27, 2022, doi:10.22541/essoar.167214177.74303978/v1
- 518 De Jonghe, J. & Keppens, R. (2020a). A two-fluid analysis of waves in a warm ion-electron
 519 plasma. *Phys. Plasmas*. 27, 122107, doi:10.1063/5.0029534

- 520 De Jonghe, J. & Keppens, R. (2020b). Two-Fluid Treatment of Whistling Behavior and the
521 Warm Appleton-Hartree Extension. *Journal of Geophysical Research: Space Physics*,
522 126, e2020JA028953, doi:10.1029/2020JA028953
- 523 De Michelis, P., Consolini, G., Alberti, T., Tozzi, R., Giannattasio, F., Coco, I., et al. (2022).
524 Magnetic Field and Electron Density Scaling Properties in the Equatorial Plasma
525 Bubbles. *Remote Sens.* 14, 918, doi:10.3390/rs14040918
- 526 De Michelis, P., Consolini, G., Tozzi, R., Pignalberi, A., Pezzopane, M., Coco, I., et al. (2021).
527 Ionospheric Turbulence and the Equatorial Plasma Density Irregularities: Scaling
528 Features and RODI. *Remote Sens.* 13, 759, doi:10.3390/rs13040759
- 529 Elias, F., Crassous, J., Derec, C., Dollet, B., Drenckhan, W., Gay, C., et al. (2020). The
530 Acoustics of Liquid Foams, *Current Opinion in Colloid & Interface Science*, 50, 10139,
531 doi:10.1016/j.cocis.2020.101391
- 532 Golkowski, M., Sarker, S.R., Renick, C., Moore, R.C., Cohen, M.B., Kulak, A., Mlyanarczyk, J.,
533 & Kubisz, J. (2018). Ionospheric D Region Remote Sensing Using ELF Sferic Group
534 Velocity. *Geophysical Research Letters*, 45, 12,739-12,748, doi:10.1029/2018GL080108
- 535 Goodman, S., Blakeslee, R., Koshak, W., Mach, D., Bailey, J., Buechler, D., et al. (2013). The
536 goes-r Geostationary Lightning Mapper (GLM). *Atmospheric Research*, 125-126, 34-49,
537 doi:10.1016/j.atmosres.2013.01.006
- 538 Goodman, S., Mach, D., Koshak, W., Blakeslee, R. (2012). Algorithm theoretical basis
539 document: GLM lightning cluster-filter algorithm. Version 3.0. July 30, 2012. NOAA
540 NESDIS Center for satellite applications research.
- 541 Heelis, R. (2004). Electrodynamics in the low and middle latitude ionosphere: A tutorial. *Journal*
542 *of Atmospheric and Solar-Terrestrial Physics*, 66(10), 825-838,
543 doi:10.1016/j.jastp.2004.01.034
- 544 Holzworth, R.H., McCarthy, M.P., Brundell, J.B., Jacobson, A.R. & Rodger, C.J. (2019). Global
545 distribution of superbolts. *Journal of Geophysical Research: Atmospheres*, 124, 9996-
546 10,005, doi:10.1029/2019JD030975
- 547 Huba, J.D. (2023). Resolution of the equatorial spread F problem: Revisited. *Front. Astron.*
548 *Space Sci.* 9:1098083, doi:10.3389/fspas.2022.1098083
- 549 Hutchins, M.L., Holzworth, R.H., Rodger, C.J., & Brundell, J.B. (2012). Far-field power of
550 lightning strokes as measured by the world-wide lightning location network. *Journal of*
551 *Atmospheric and Oceanic Technology*, 29, 1102-1110. [https://doi.org/10.1175/JTECH-D-](https://doi.org/10.1175/JTECH-D-11-00174.1)
552 11-00174.1
- 553 Hysell, D.L., Larsen, M.F., Swenson, C.M., Barjatya, A., Wheeler, T.F., Sarango, M.F., et al.
554 (2005). Onset conditions for equatorial spread F determined during EQUIS II.
555 *Geophysical Research Letters*, 32 (L24104), doi:10.1029/2005GL024743
- 556 Immel, T.J., Mende, S.B., Frey, H.U., Peticolas, L.M., & Sagawa, E. (2003). Determination of
557 low latitude plasma drifts speeds from FUV images. *Geophysical Research Letters*,
558 30(18), 1945, doi:10.1029/2003GL017573
- 559 Jackson, J.D. (1975). *Classical Electrodynamics*. New York: John Wiley & Sons.
- 560 Jacobson, A.R., Holzworth, R.H., Pfaff, R. & Roderick H. (2018). Coordinated Satellite
561 Observations of the Very Low Frequency Transmission Through the Ionospheric D Layer
562 at Low Latitudes, Using Broadband Radio Emissions from Lightning. *Journal of*
563 *Geophysical Research: Space Physics*, 123, 2926-2952, doi:10.1002/2017JA024942
- 564 Kelley, M.C., Makela, J.J., de La Beaujardiere, O., & Retterer, J. (2011). Convective Ionospheric
565 Storms: A Review. *Rev. Geophys.*, 49, RG2003, doi:10.1029/2010RG000340

- 566 Karan, D.K., Daniell, R.E., England, S.L., Martinis, C.R., Eastes, R.W., Burns, A.G., &
567 McClintock, W.E. (2020). First zonal drift velocity measurement of equatorial plasma
568 bubbles (EPBs) from a geostationary orbit using GOLD data. *Journal of Geophysics:
569 Space Physics* 125, e2020JA028173, doi:10.1029/2020JA028173
- 570 Kil, H., Demajistre, R., & Paxton, L.J. (2004). F-region plasma distribution seen from
571 TIMED/GUVI and its relation to the equatorial spread F activity. *Journal of Geophysical
572 Research*, 31, L05810, doi:10.1029/2003GL018703
- 573 Kil, H., & Heelis, R.A. (1998). Global distribution of density irregularities in the equatorial
574 ionosphere. *Journal of Geophysical Research*, 103, 407-417 doi:10.1029/97JA02698
- 575 Kil, H., Sun, K.A., Chang, H., Paxton, L.J., Nikoukar, R., & Lee, J. (2022). Characteristics and
576 sources of electron density irregularities near and after midnight in the equatorial F
577 region. Oral presentation SA55A-03 at AGU fall meeting, Chicago Illinois, USA.
578 <https://agu.confex.com/agu/fm22/meetingapp.cgi/Paper/1177560>
- 579 Kudeki, E., & Bhattacharyya, S. (1999). Postsunset vortex in equatorial F-region plasma drifts
580 and implications for bottomside spread F. *Journal of Geophysical Research*, 104(A12),
581 28, 163-28, 170, doi:10.1029/1998JA900111
- 582 Liang, J., Donovan, E., Jackel, B., Spanswick, E. & Gillies, M. (2016) On the 630 nm red-line
583 pulsating aurora: Red-line Emission Geospace Observatory observations and model
584 simulations. *Journal of Geophysical Research: Space Physics*, 121, 79880-8012,
585 doi:10.1002/2016JA022901
- 586 Makela, J.J., & Kelley, M.C. (2003). Field-aligned 777.4-nm composite airglow images of
587 equatorial plasma depletions. *Geophysical Research Letters*, 30(8), 1442,
588 doi:10.1029/2003GL017106
- 589 Makela, J.J., Kelley, M.C., & Nicolls, M.J. (2006). Optical observations of the development of
590 secondary instabilities on the eastern wall of an equatorial plasma bubble, *J. Geophys.
591 Res.*, 111, A09311, doi:10.1029/2006JA011646
- 592 Makela, J.J. & Miller, E.S. (2008). Optical observations of the growth and day-to-day variability
593 of equatorial plasma bubbles, *J. Geophys. Res.*, 113, A03307,
594 doi:10.1029/2007JA012661
- 595 Makela, J.J. & Otsuka, Y. (2012). Overview of Nighttime Ionospheric Instabilities at Low- and
596 Mid-Latitudes: Coupling Aspects Resulting in Structuring at the Mesoscale. *Space Sci.
597 Rev* 168, 419-440, doi:10.1007/s11214-011-9816-6
- 598 Martinis, C., Eccles, J.V., Baumgardner, J., Manzano, J., & Mendillo, M. (2003). Latitude
599 dependence of zonal plasma drifts obtained from dual-site airglow observations. *Journal
600 of Geophysical Research*, 108(A3), 1129, doi:10.1029/2002JA009462
- 601 Mendillo, M., & Baumgardner, J. (1982). Airglow characteristics of equatorial plasma
602 depletions. *Journal of Geophysical Research*, 87(A9), 7641-7652,
603 doi:10.1029/JA087iA09p07641
- 604 Min, K., Takahashi, K., Ukhorskiy, A.Y., Manweiler, J.W., Spence, H.E., Singer, H.J., et al.
605 (2017), Second harmonic poloidal waves observed by Van Allen Probes in the dusk-
606 midnight sector. *J. Geophys. Res. Space Physics*, 122, 3013-3039,
607 doi:10.1002/2016JA023770
- 608 Narayanan, V.L., Sau, S., Gurubaran, S., Shiokawa, K., Balan, N., & Emperumal, K. (2014). A
609 statistical study of satellite traces and subsequent evolution of equatorial spread F based
610 on ionosonde observations over dip equatorial site Tirunelveli, India. *Earth, Planets and
611 Space*, 676(1), 160, doi:10.1186/s40623-014-0160-4

- 612 Nickolaenko, A.P., & Rabinowicz, L.M. (2004). Time domain presentation for ELF pulses with
613 accelerated convergence. *Geophysical Research Letters*, 31, L05808,
614 doi:10.1029/2003GL018700
- 615 Patra, A.K., Yokoyama, T., Yamamoto, M., Saito, S., Maruyama, T. & Fukao, S. (2005).
616 Disruption of E region echoes observed by the EAR during the development phase of
617 equatorial spread F: A manifestation of electrostatic field coupling. *Geophysical*
618 *Research Letters*, 32(L17104), doi:10.29/2005GL022868
- 619 Pierre, J., Guillermic, R., Elias, R., Drenckhan, W., & Leroy, V. (2013). Acoustic
620 characterization of liquid foams with an impedance tube. *The European Physical Journal*
621 *E* 36(113), doi:10.1140/epje/i2013-13113-1
- 622 Piggott, W.R. & Rawer, K. (1972). URSI Handbook of Ionogram Interpretation and Reduction,
623 second Edition, November 1972, WDC A, Report UAG-23.
624 <https://repository.library.noaa.gov/view/noaa/10404>
- 625 Pimenta, A.A., Bittencourt, J.A., Fagundes, P.R., Sahai, Y., Buriti, R.A., Takahashi, H., &
626 Taylor, M.J. (2003). Ionospheric plasma bubble zonal drifts over the tropical region: A
627 study using OI 630 nm emission all-sky images. *Journal of Atmospheric and Solar-*
628 *Terrestrial Physics*, 65(10), 1117-1126, doi:10.1016/S1364-6826(03)00149-4
- 629 Ripoll, J.F., Farges, T., Malaspina, D.M., Lay, E.H., Cunningham, G.S., Hospodarsky, G.B. et al.
630 (2020), Analysis of Electric and Magnetic Lightning-Generated Wave Amplitudes
631 Measured by the Van Allen Probes. *Geophysical Research Letters*, 47, e2020GL087503,
632 doi:10.1029/2020GL087503
- 633 Ritter, P., Luhr, H., & Rauberg, J. (2013), Determining field-aligned currents with the Swarm
634 constellation mission. *Earth Planets Space*, 65, 1285-1294, doi:10.5047/eps.2013.09.006
- 635 Rodriguez-Zuluaga, J., Stolle, C., Yamazaki, Y., Xiong, C., & England, S.L. (2020). A synoptic-
636 scale wavelike structure in the nighttime equatorial ionization anomaly. *Earth and Space*
637 *Science*, 8, e2020EA001529, doi:10.1029/2020EA001529
- 638 Rudlosky, S., Goodman, S., Virts, K., & Bruning, E. (2019). Initial Geostationary Lightning
639 Mapper observations. *Geophysical Research Letters*, 46, 1097-1104,
640 doi:10.1029/2018GL081052
- 641 Santolik, O., Parrot, M., & Lefeuvre, F. (2003). Singular value decomposition methods for wave
642 propagation analysis. *Radio Science*, 38(1), 1010, doi:10.1029/2000RS002523
- 643 Shiokawa, K., Otsuka, Y., Ogawa, T., & Wilkinson, P. (2004). Time evolution of high-altitude
644 plasma bubbles imaged at geomagnetic conjugate points. *Annales Geophysicae*, 29(9),
645 3137-3143, doi:10.5194/angeo-22-3137-2004
- 646 Sivakandan, M., Mondal, S., Sarkhel, S., Chakrabarty, D., Sunil Krishna, M., V. Upadhyaya,
647 A.K., et al. (2021). Evidence for the in-situ generation of plasma depletion structures over
648 the transition region of geomagnetic low-mid latitude. *Journal of Geophysical Research:*
649 *Space Physics*, 126, e2020JA028837, doi:10.1029/2020JA028837
- 650 Tsunoda, R.T. (1983). On the generation and growth of equatorial backscatter plumes: 2.
651 Structuring of the west walls of upwellings. *Geophysical Research Letters*, 88(A6), 4869-
652 4874, doi:10.1029/JA088iA06p04869
- 653 Wood, A.B. (1941). Textbook of Sound: Being an Account of the Physics of Vibrations with
654 Special Reference to Recent Theoretical and Technical Developments, Second Edition,
655 page 361, Macmillan Co., New York.
- 656 Woodman, R.F. (2009). Spread F - an old equatorial aeronomy problem finally resolved? *Ann.*
657 *Geophysics* 27(5), 1915-1934, doi:10.5194/angeo-27-1915-2009

658 Woodman, R.F. and Hoz, C.L. Radar Observations of F Region Equatorial Irregularities. *Journal*
 659 *of Geophysical Research*, 81(31), 5447-5466, doi:10.1029/JA081i031p05447
 660 Yokoyama, T., Yamamoto, M., Otsuka, Y., Nishioka, M., Tsugawa, T., Watanabe, S., & Pfaff,
 661 R.F. (2011). On postmidnight low-latitude ionospheric irregularities during solar
 662 minimum: 1. Equatorial Atmosphere Radar and GPS-TEC observations in Indonesia.
 663 *Journal of Geophysical Research*, 116, A11325, doi:10.1029/2011JA016797
 664 Zheng, H., Holzworth, R.H., Brundell, J.B., Jacobson, A.R., Wygant, J.R., Hospodarsky, G.B.,
 665 Mozer, F.S., & Bonnell, J. (2015). A statistical study of whistler waves observed by Van
 666 Allen Probes (RBSP) and lightning detected by WWLLN. *Journal of Geophysical*
 667 *Research: Space Physics*, 121, 2067-2079, doi:10.1002/2015JA022010

668
 669

670 **Figure 1.** Scalograms (in **a**, **c**, and **e**) and time resolved plots (**b**, **d**, and **f**) of the electric field
 671 components are shown for a period while VAP-A passes through the root of a plasma bubble. In
 672 (**g**) the summation of the radial electric field contributions from all WWLLN detected lightning
 673 strokes within this time interval using the (Nickolaenko et al., 2004) model with WWLLN
 674 determined amplitudes is plotted. The percentage values shown above the three peaks in **f**
 675 represent the ratios of the observed peak amplitudes to the model amplitudes of the
 676 corresponding peaks seen in (**g**). The predicted arrival times at the subsatellite location using
 677 WWLLN/GLM stroke times are shown by the red/white dashed vertical lines in (**a**, **c** and **e**). The
 678 GLM times appear systematically later by 2 ms than the WWLLN times. The second of the
 679 peaks in (**f**) was seen by GLM but not detected by WWLLN. In the scalograms, some extraneous
 680 radio frequency interference at approximately 2 kHz and harmonics can be seen. The geographic
 681 location of the subsatellite point at the start of this data burst is shown in the title. Also shown is
 682 the location of the flash responsible for the four peaks in (**f**). The angular difference between
 683 these locations along the great circle is shown as $\Delta\theta$.

684

685 **Figure 2.** Scalograms and time resolved plots of VAP-A data with the same layout as in the
 686 previous figure are shown for a different period. The percentage values shown above the three
 687 peaks in (**f**) represent the ratios of the observed peak amplitudes to the model amplitudes of the
 688 corresponding peaks seen in (**g**). As in the previous figure, and in similar subsequent figures, the
 689 angular distance along the great circle containing both the satellite location and the relevant
 690 lightning flash location is indicated by the value of $\Delta\theta$ in the figure title.

691

692 **Figure 3.** Scalograms of the three magnetic and electric field components in the spinning U,V,
 693 W reference frame are displayed for a 1.6 s sample of EMFISIS data. The dashed line curves
 694 represent four distinct dispersion constant (DC) values that track the dispersed waves from a
 695 single lightning stroke detected by the WWLLN. In (a, b and c), scalograms for the Bu, Bv and
 696 Bw components of the magnetic field are shown. In d, e and f, scalograms for the Eu, Ev and Ew
 697 components of the electric field are shown. The approximate location and local solar time (LST)
 698 of the satellite at the time of this data collection is shown in the figure title.

699 **Figure 4.** The direction and speed for four different DC values are displayed for points along
 700 each of the dispersion curves shown in the previous figure. In (a, f, k and p), the absolute values
 701 for the projections of the Poynting unit vector \mathbf{S} along $\boldsymbol{\mu}$ (the direction of the local magnetic field
 702 \mathbf{B}) are plotted as a function of frequency. Similarly in (b, g, l and q), projections along the \mathbf{v}
 703 direction (approximately vertical) of the MFA coordinate system are shown. Also similarly in (c,
 704 h, m and r), projections along the ϕ direction (magnetic East) of the MFA coordinate system are
 705 shown. In (d, i, n, s), the magnitudes of the electric and magnetic field amplitudes are shown as a
 706 function of frequency. In (e, j, o, and t) the RPA estimated phase velocities are plotted as a
 707 function of frequency.
 708

709 **Figure 5.** Scalograms of the three magnetic and electric field components in the spinning U,V,
 710 W reference frame are displayed for a single burst of EMFISIS data. The white dashed vertical
 711 lines are plotted at the times of the arrival at the subsatellite location for every WWLLN event
 712 detected during this data burst. In (a, b and c), scalograms for the Bu, Bv and Bw components of
 713 the magnetic field are shown. In (d, e and f), scalograms for the Eu, Ev and Ew components of
 714 the electric field are shown. In (g), the satellite spin vector coordinates λ (in the fashion of
 715 latitude) and δ (in the fashion of longitude), characterizing the spin vector orientation relative to
 716 the local magnetic field, are indicated over the course of this data burst. The approximate
 717 location and local solar time (LST) of the satellite at the start of this data burst is shown in the
 718 legend for section (g).
 719

720 **Figure 6.** Scalograms for the indicated subset of the time range in the previous figure are shown
 721 here. In (a, b and c), scalograms of the three magnetic field components are shown. In (d, e and
 722 f), scalograms of the three electric field components are shown. In (f), the arc distances, (80° ,
 723 18° , 162° and 79°), along the great circle containing the subsatellite location and the four
 724 WWLLN stroke locations are shown in blue text labels near the four dashed red vertical lines for
 725 the estimated arrival times at the subsatellite location of the four WWLLN strokes. The first two
 726 strokes appear sufficiently isolated that they may be tentatively identified with the scalogram
 727 spikes labelled #1 and #2 in (f).

728 **Figure 7.** A wavevector analysis with the same layout as that displayed in Figure 4 is shown here
729 for the four times indicated in Figure (6f) by white vertical dashed lines and numbered #3, #4, #5
730 and #8. The locally dispersionless nature of the scalogram peaks seen in Figure 6 is validated by
731 the nearly constant phase velocity values above the local Oxygen cyclotron frequency seen
732 especially clearly in (e and o).

733 **Figure 8.** A physical model of a region of “foamy plasma” near the bottom of the ionosphere is
734 illustrated. A sketch of the “Wood’s law” derivation of the estimated speed of sound in the two-
735 phase mixture is shown.

736 **Figure 9.** The variation of dispersionless pulse attenuation as a function of propagation delay
737 through foamy plasma is plotted. The two points with error bars shown represent the two cases
738 displayed in Figures 1 and 2 above.

739

Figure 1.

Viewpoint: -2.5°N -154.6°E Alt 238.6km V(EIWG)= 245 km/s Single Flash 4 Strokes @ 9.2°N 84.8°W $\Delta\theta=71^\circ$

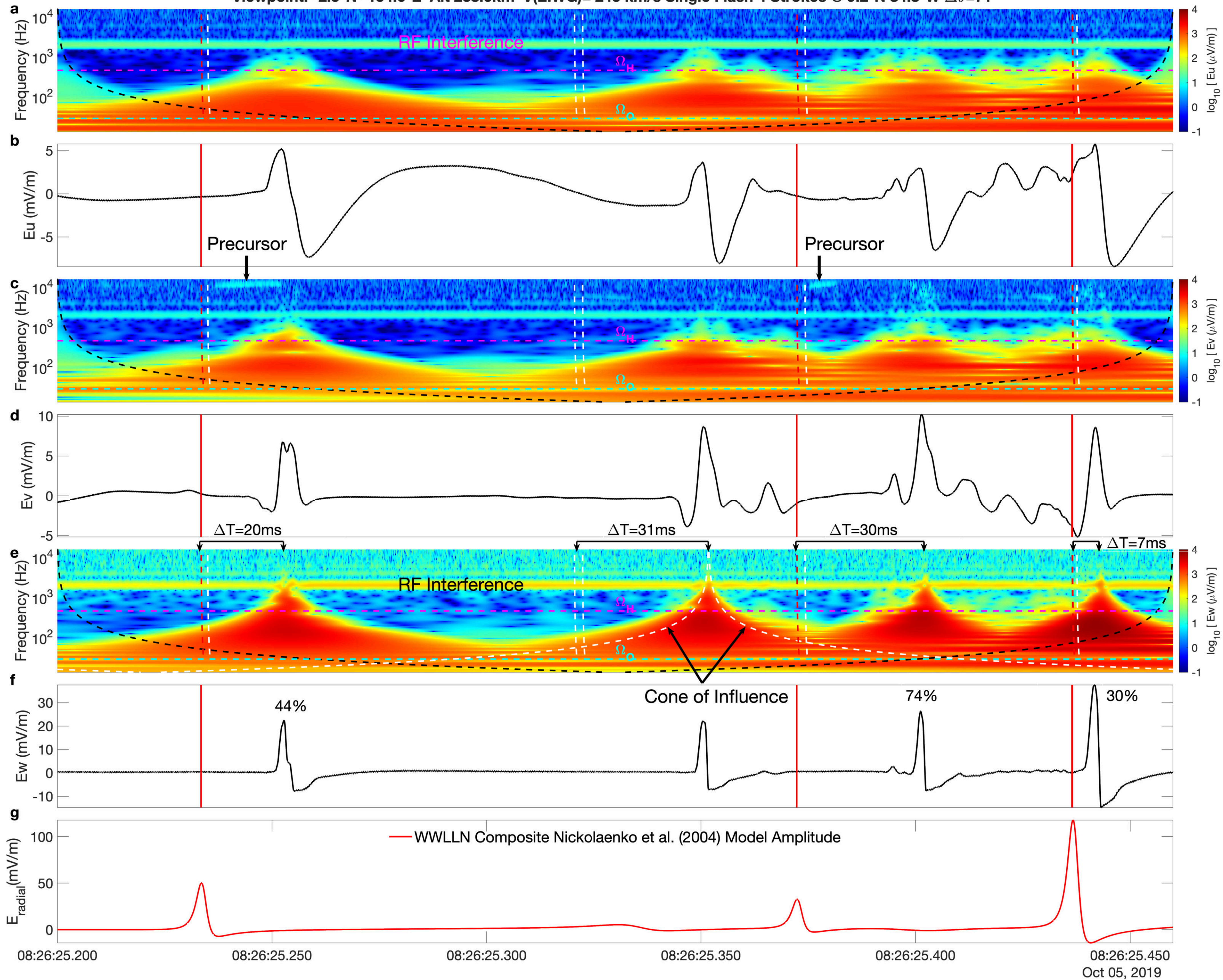


Figure 2.

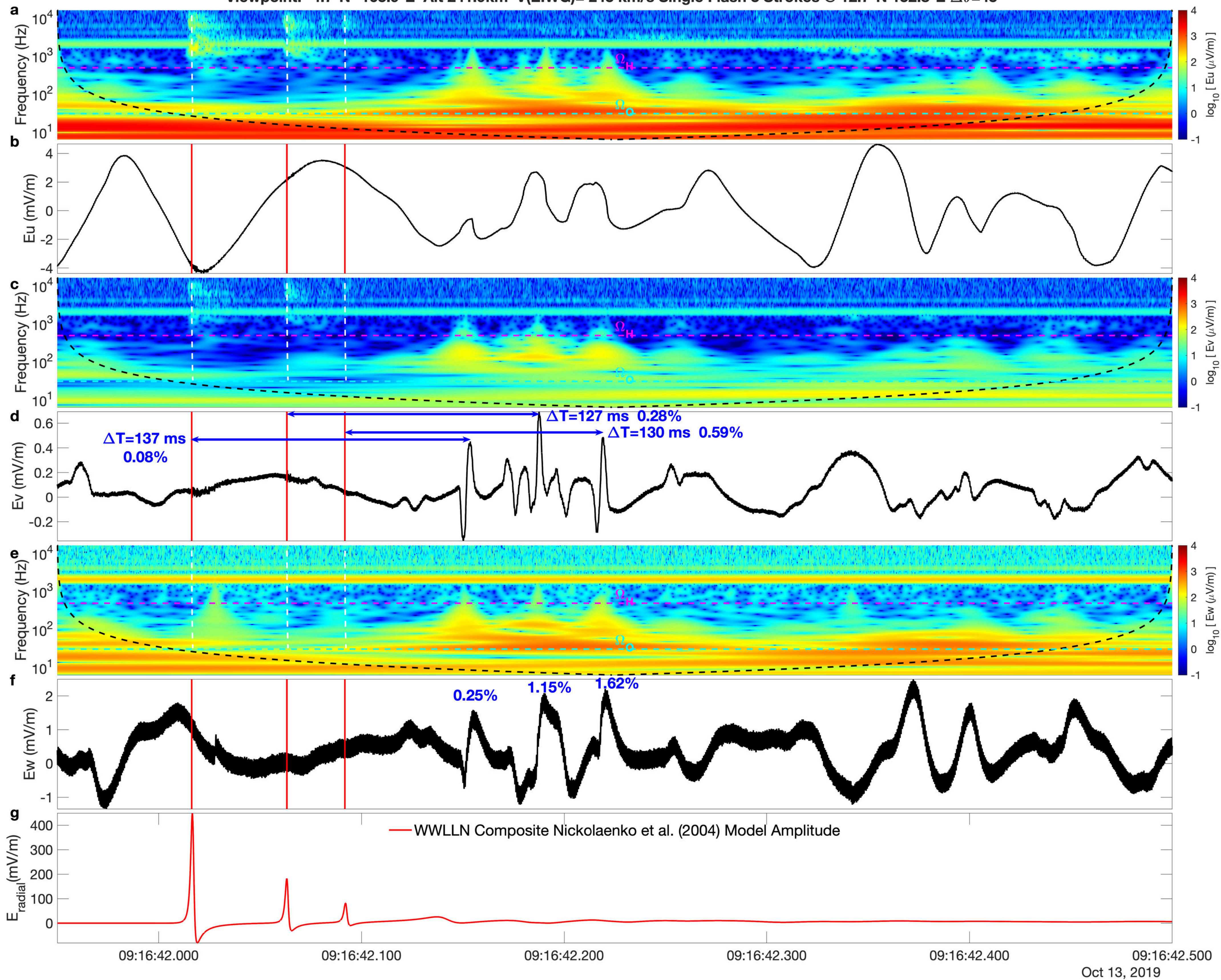


Figure 3.

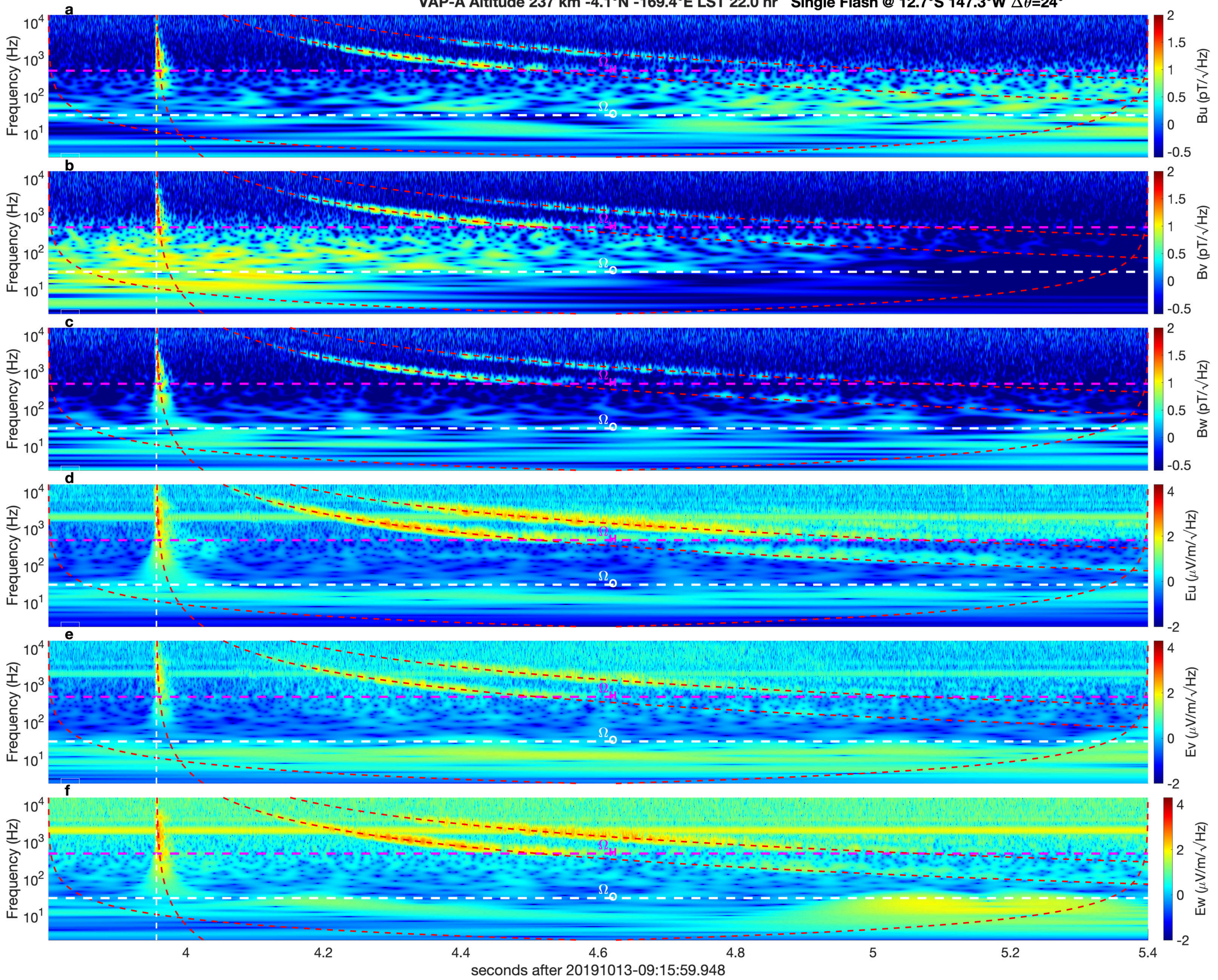


Figure 4.

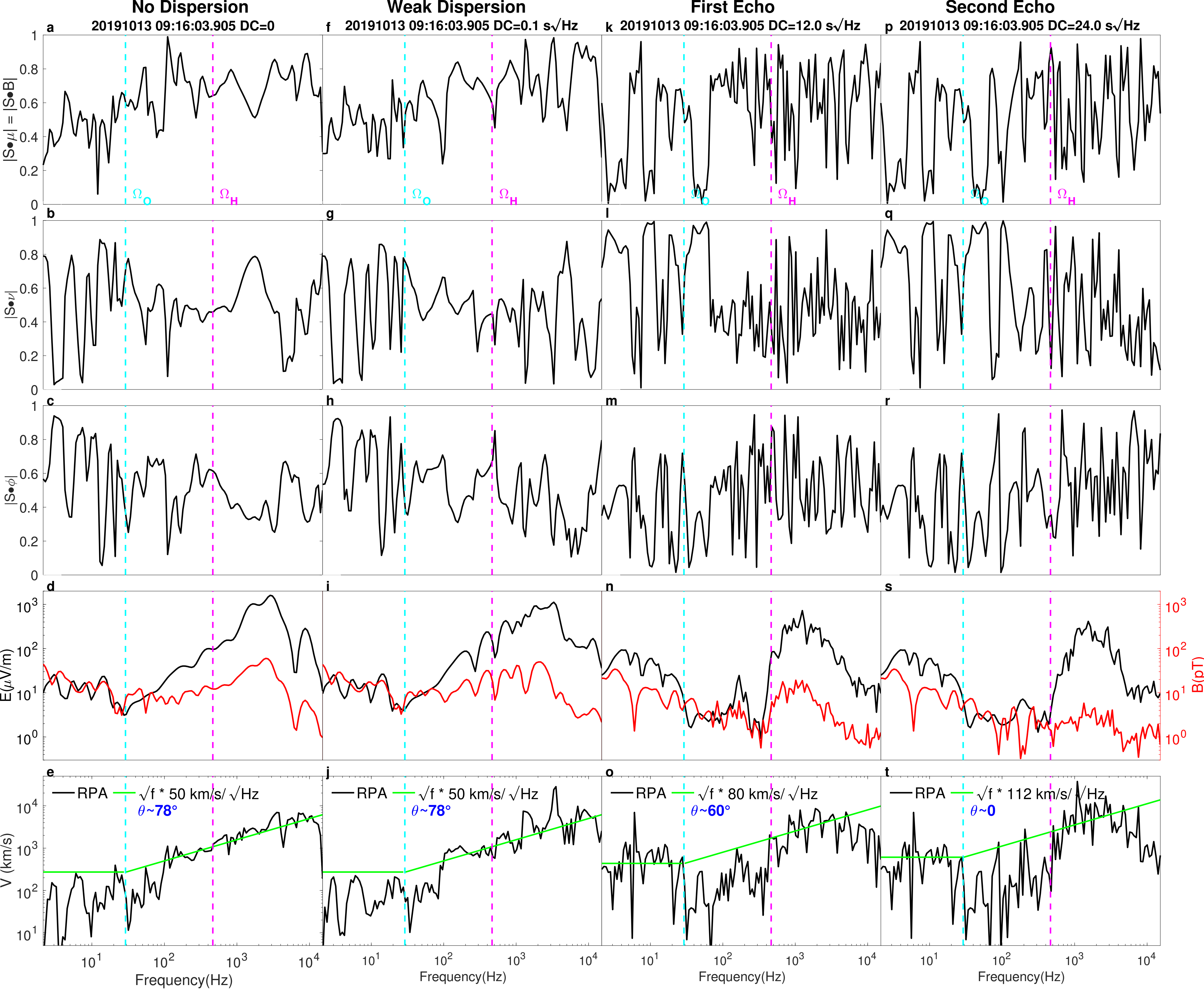


Figure 5.

Magnetic & Electric Field Scalograms

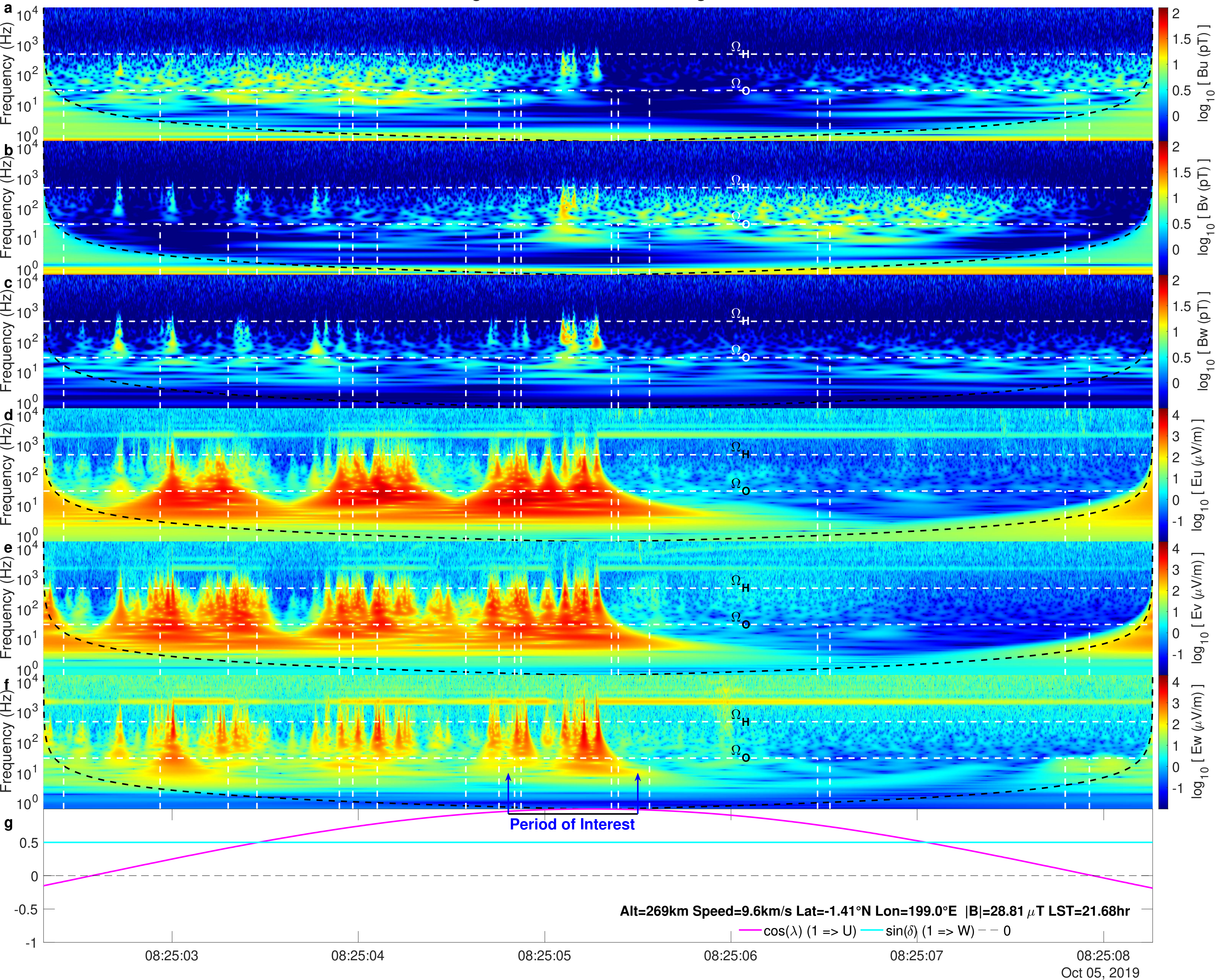


Figure 6.

VAP-A Altitude 269 km -1.4°N -161.0°E LST 21.7 hr

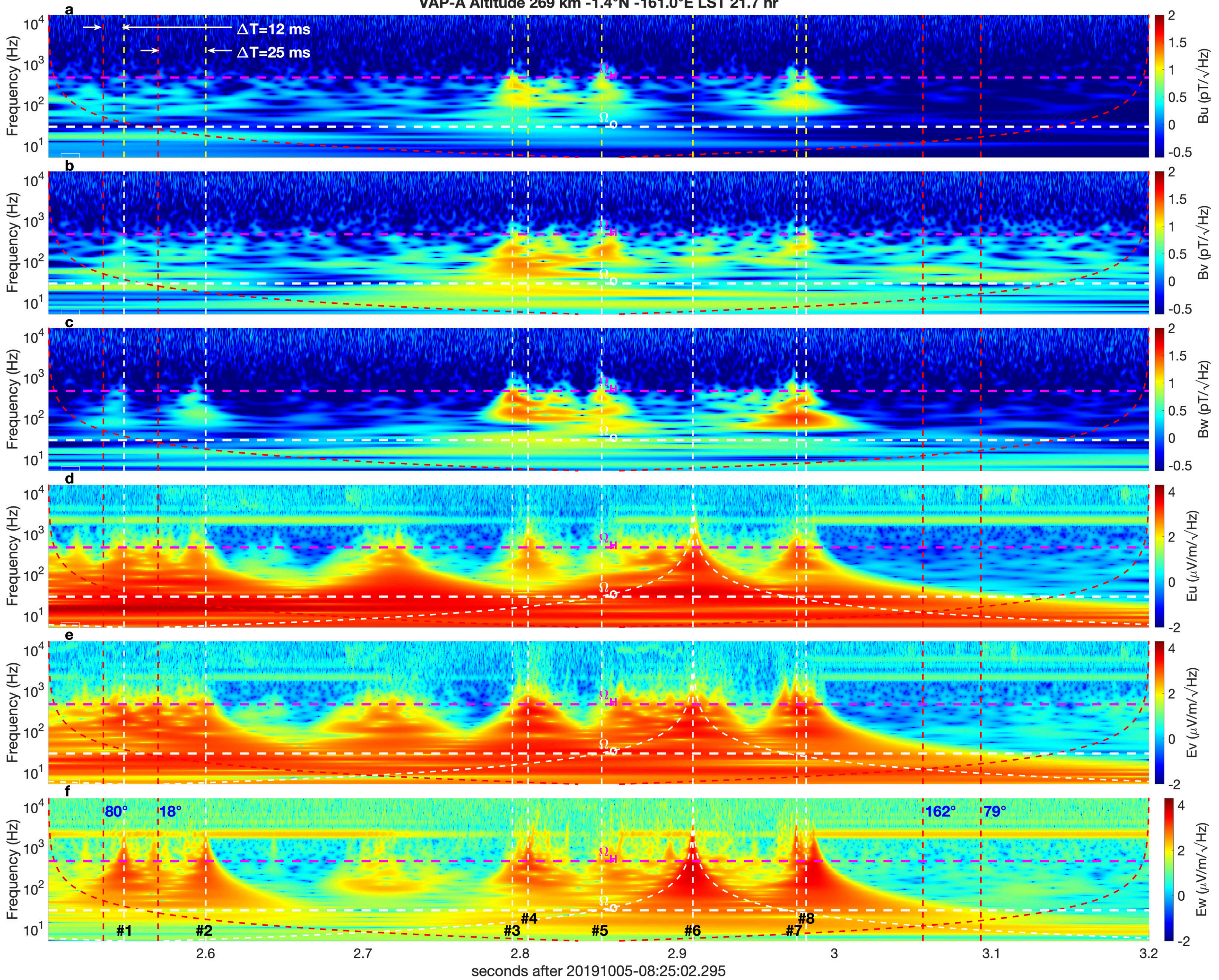


Figure 7.

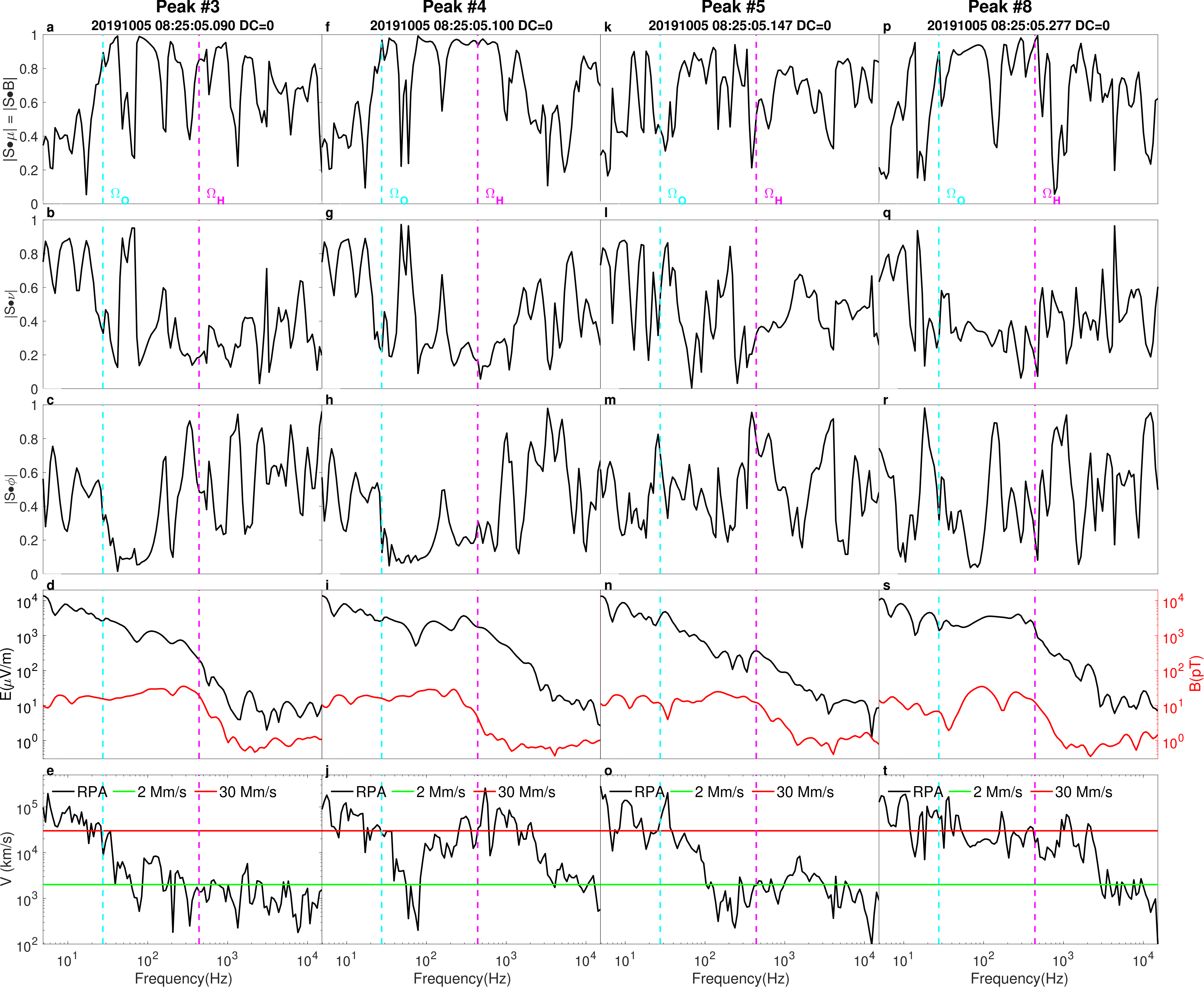
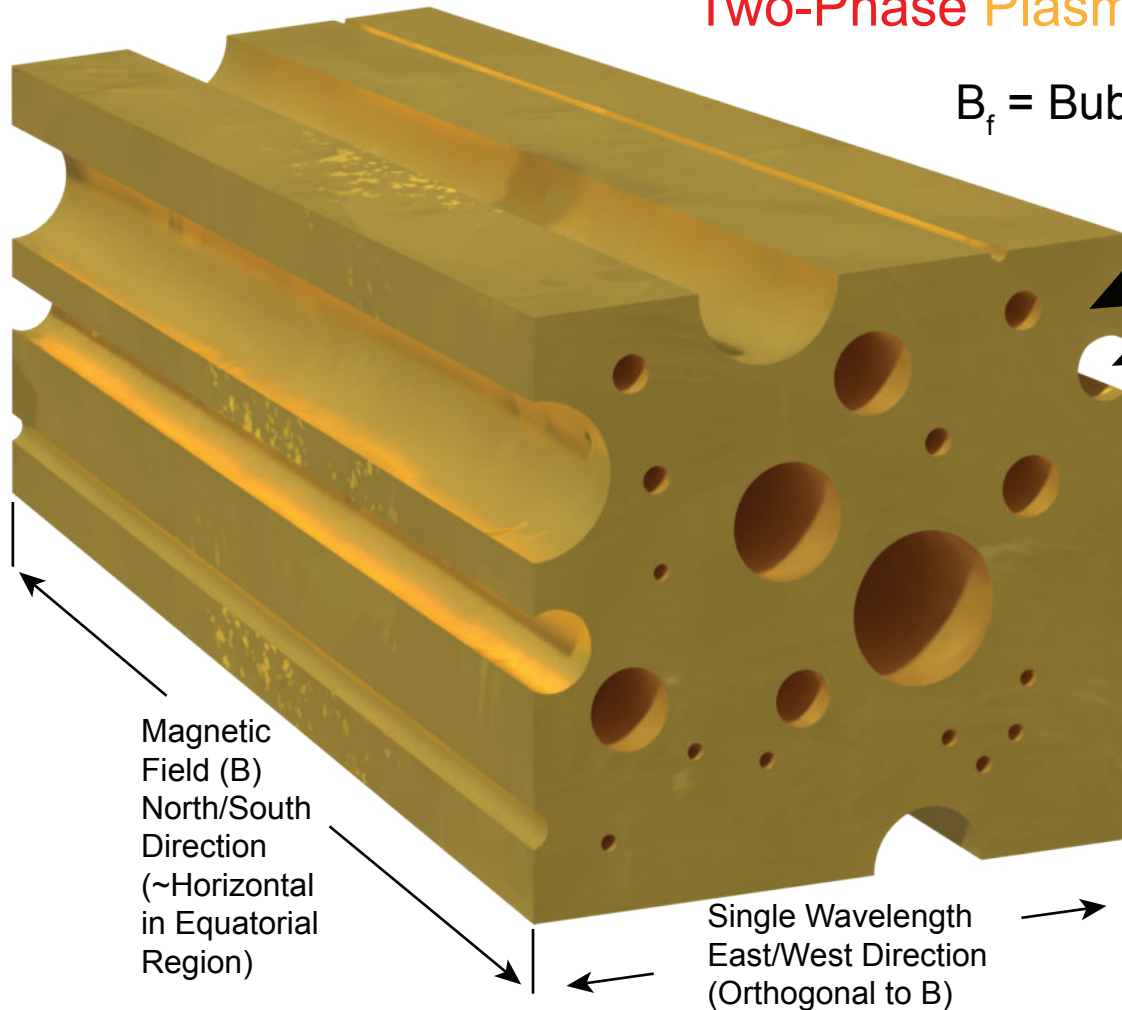


Figure 8.

Speed of Sound in "Foamy" Two-Phase Plasma/Bubble Mix



B_f = Bubble Volume Fraction

Densities

$$\rho_{\text{Plasma}} \gg \rho_{\text{Bubble}}$$

Compressibilities

$$\chi_{\text{Plasma}} \ll \chi_{\text{Bubble}}$$

Mixture Density

$$\rho_{\text{Mix}} = (1-B_f) \rho_{\text{Plasma}} + B_f \rho_{\text{Bubble}}$$

Mixture Compressibility

$$\chi_{\text{Mix}} = (1-B_f) \chi_{\text{Plasma}} + B_f \chi_{\text{Bubble}}$$

Magnetic Field (B)
North/South
Direction
(~Horizontal
in Equatorial
Region)

Single Wavelength
East/West Direction
(Orthogonal to B)

$$V_{\text{Mix}} = \frac{1}{\sqrt{\rho_{\text{Mix}} \chi_{\text{Mix}}}} \approx \frac{1}{\sqrt{(1-B_f) B_f \rho_{\text{Plasma}} \chi_{\text{Bubble}}}} < V_{\text{Plasma}} \quad \& \quad < V_{\text{Bubble}}$$

"Wood's Law"

Figure 9.

